Supporting Information for *Variation of hydraulic properties due to dynamic fracture damage: Implications for fault zones*

Franciscus M. Aben*, Mai-Linh Doan†, and Thomas M. Mitchell

Contents of this file

1. Text S1 to S3
2. Figures S1 to S4
3. Table S1

Introduction The supporting information consists of an explanation for the picking of the yield point from the dynamic loading tests (Text S1, Figures S1 and S2), the approach for calibrating the storage capacity (Text S2, Figure S3), the results for the *P*-wave velocity (Text S3, Figure S4), and the permeability at varying effective pressure data in tabulated form (Table S1).

Text S1. Establishing yield point in dynamic loading tests

Rocks subjected to compressive loading in the brittle field typically experience three phases before macroscopic failure at the peak stress: a) closure of cracks parallel to the direction of loading at low stresses, b) elastic deformation up to about two-thirds of the peak stress, followed by c) dilation and stable propagation of cracks called the elastic yield point (**?**). At a certain length, crack propagation becomes unstable and causes macroscopic failure of the rock at the peak stress. These pre-failure processes have been studied extensively under quasi-static conditions (i.e. at strain rates $\dot{\varepsilon} < 10^{-5}$ s^{-1}).

In case of our experiments, the achieved peak stress is not necessarily similar to the peak stress at failure because 1) the samples did not fail during loading, or 2) the loading duration was too short to reach the highest possible dynamic peak stress. The yield point however is often reached during high strain rate experiments, if any damage has accumulated in the sample. Thus, rather than trying to define a (possibly wrong) failure peak stress, we aim to define the yield point.

Another advantage of defining a yield point in high strain rate experiments is that the strain rate sensitivity of brittle materials can be expressed in a yield strain rate; the strain rate experienced by the sample at the moment of yielding. The stress and strain rate are never constant during a dynamic high strain rate loading test on split Hopkinson pressure bar apparatus, thus defining a 'critical' strain rate for each test remains problematic and varies from one study to the other. For instance, strain rates have been defined as an average strain rate (**?**), as the peak strain rate excluding the strain rate peak that may occur after sample pulverisation (**???**), as the constant strain rate 'plateau' observed after an initial strain rate peak (**??**) (one needs a very smooth incident stress wave with a long loading duration), or not defined at all.

In this appendix, we present how to obtain the elastic yield points from experimental SHPB data on crystalline rock. We define the yield point from high speed camera footage. This visually determined yield point coincides with the deflection from elastic linearity in the mechanical data, and thus supports our determination of the yield point from the mechanical data. This analyses had been applied to the published data of **?** as well, but below we present more rigorous support.

A high speed camera (Photron SA5) was used in conjunction with the mini-split Hopkinson pressure

*Department of Earth Sciences, UCL, UK, f.aben@ucl.ac.uk
†ISTerre, Université Grenoble Alpes, Grenoble, France

bar to define the visual yield point of some quartz monzonite samples (the mechanical data from these tests were not included in this manuscript, and these samples were not subjected to post-mortem characterisation). The camera was connected to the acquisition system of the SHPB to synchronise the mechanical data and the camera footage. The camera footage was stored after the camera was triggered by the same laser used to trigger the SHPB acquisition system. The frame rate was set at 300k fps, giving a grey image with a resolution of 128 by 64 pixels. Two nominally dry quartz-monzonite samples (numbered GT13, GT15 and GT16, dimension 10 by 10 mm) were subjected to high strain rate loadings. A steel striker (20 cm length) was used in combination with cardboard pulse shapers. The striker velocity was 3.6 m/s and 3.7 m/s for sample GT15 and GT16 respectively. Both samples were pulverised and a second strain rate peak was observed in the mechanical data.

The elastic yield point, defined by the moment of fracture initiation, was established from the footage by subtracting the frames of the sample in rest (before the arrival of the incident stress wave) from the remaining frames including those shot during sample deformation. To do so, a mean grey value image was calculated from the first 50 frames and subtracted from the rest of the data. A non-zero value of a pixel represents a change in light intensity, which we interpret as movement or change of the sample and bar surfaces. Figure A1 shows the result of this simple analysis for the mean change of 23 rows of pixels across the sample over time. Some local changes become apparent over a time interval t_{yield} to t_{fail}, followed by extensive pervasive deformation. The synchronised strain rate data indicates that the onset of the extensive deformation at t_{fail} corresponds with an increase towards the second strain rate peak (Figure A1) related to overall pulverisation of the sample. Thus, we interpret the time interval that precedes macroscopic failure (t_{yield} to t_{fail}) as the phase between the yield point and the peak failure stress. Hence, the onset of this pre-failure stage is the yield point t_{yield}.

The yield point established from the high speed camera footage matches the approximate yield point established from mechanical data. This mechanical yield point is the deflection from linear elasticity, but it can be challenging to define this in low strain rate mechanical data, let alone for dynamic loading data. Here, we interactively pick the yield point from the stress-strain curve (Figure A2b) and support this by looking at the stress, strain, and strain rate history (Figure A2b), and the stress-strain ratio and it's time derivative (Figure A2c). These last two ratio's effectively represent Young's modulus over time, thus deviation from a (more or less) constant value indicates the yield point. This approach was used for all the mechanical loading data obtained in this study, and we have prescribed an error in the pick of the yield point of ± 3 μs.

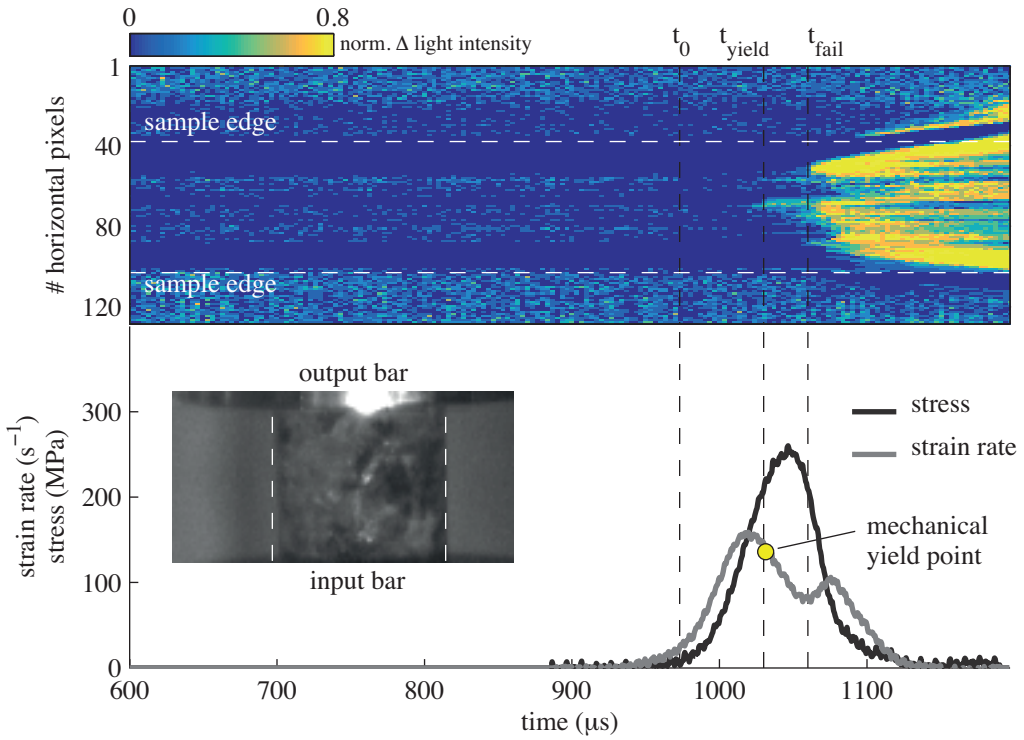

Figure 1: Top: Normalised change in mean light intensity (absolute change in grey value) of 23 rows of pixels across the sample versus time. Bottom: the stress and strain rate history experienced by the sample. t_0, t_{yield}, and t_{fail} represent the onset of loading, the onset of yielding, and the macroscopic failure (pulverisation in this case) of the sample, respectively.

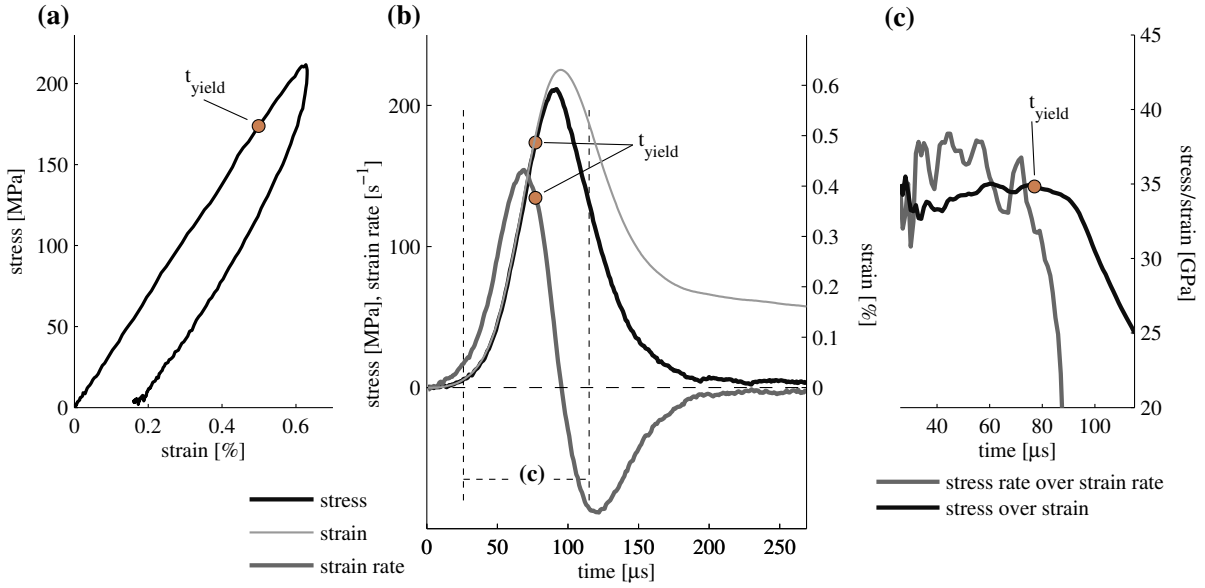

Figure 2: (a): Stress-strain curve for a high strain rate experiment. t_{yield} represent the yield point established from (b) and (c). (b): Stress, strain, and strain rate history of the same high strain rate experiment shown in (a). The time interval shown in (c) is highlighted. (c): The stress-strain ratio and stress rate - strain rate ratio over time shows where the mechanical data diverges from linear elastic behaviour at t_{yield}.

Text S2. Calibration for storage capacity

The storage capacity was calculated as shown in the main text. To obtain ΔV_{pf} for the sample only, the volume change of the sample holder setup was subtracted from the measured amount of expelled pore fluid. This calibration was done twice because two sample holder setups were used, one for less damaged samples with a size adapter of 15 mm diameter (Figure B1), and one for more damaged samples with a size adapter of 18 mm. The two setups contain different pore fluid distribution plates and porous discs (Figure B1). The amount of expelled fluid from the samples holders was measured by using the same approach described in the main text for the samples, only without actual sample in the setup.

For the 18 mm diameter setup the amount of fluid expelled by the system only is $7.50 \times 10^{-16}\,\mathrm{m^3Pa^{-1}}$, measured at the highest effective pressures (25-35 MPa). This number is the sum of the fluid expelled from half the system connected to the open pore fluid intensifier and half the system connected to the closed pore fluid intensifier. Samples measured in this sample holder were (nearly) pulverised and had very high permeabilities (Figure 4). Therefore we assume that they were not flow barriers and the fluid from the closed half of the system was allowed to pass through the sample in the short time (seconds) that the 'instantaneous' fluid expulsion was measured.

For the 15 mm diameter sample setup the fluid expelled by system only is $9.4{-}10{\times}10^{-16}\,\mathrm{m^3Pa^{-1}}$, measured at the highest effective pressures (25-35 MPa). Using this value on the lower permeability samples yielded negative values for the drained modulus. Thus, the fluid expelled by the closed half of the system did not flow through the sample during the short duration of a confining pressure step. A dummy steel sample was used as an impermeable sample that compartmentalised the system. The fluid expelled by each half of the system was then measured and yielded $5.46{\times}10^{-16}\,\mathrm{m^3Pa^{-1}}$ and $3.65{\times}10^{-16}\,\mathrm{m^3Pa^{-1}}$ for each half respectively. A reason for dissimilar values for both halves might be that one half has a large length of high pressure tubing within the confining pressure vessel, while the other half has a direct short pathway out of the confining pressure vessel. Using either of the two values for the low permeability samples yields realistic drained moduli.

For 'intermediate' permeability samples (i.e. sample QM16, QM17), a small amount of pore fluid from the closed half of the system will flow through the sample during measurement. Hence, the values above are end-member values for these samples, effectively giving a range of possible storage capacities. This range, for sample QM17, is $3.4 \times 10^{-10}\,\mathrm{Pa^{-1}}$ (sample acts as an impermeable barrier) to $1.1 \times 10^{-10}\,\mathrm{Pa^{-1}}$ (sample is highly permeable). For lower and higher permeable samples the error range decreases since it yields negative storage capacities when low permeable samples act in an 'open' system, and high permeable samples expel enough fluid relative to the fluid expelled from the system only. Hence, the specific storage capacities of the highest permeable (pulverised) samples are most robust, the other specific storage capacities are order-of-magnitude values.

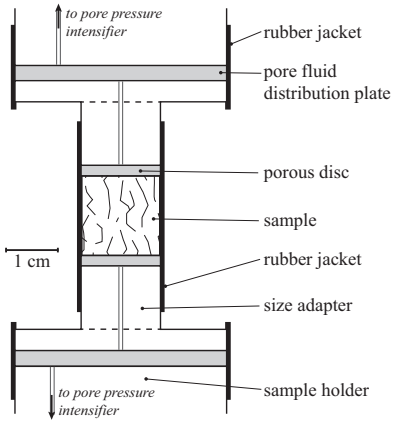

Figure 3: Schematic for the setup to calibrate the storage capacity of the permeameter.

Text S3. *P*-wave velocity

P-wave velocity was measured on the same subset of samples on which permeability was measured. The end-caps of the permeameter contained 1 MHz piezoelectric *P*-wave transducers. A signal was excited at one of the transducers, and recorded by the receiving transducer. The waveforms were digitally stored, and the *P*-wave arrival was picked manually. The *P*-wave velocity was obtained from the sample length and the time-of-flight, corrected for travel time through the pore fluid distribution plates and the sample holder.

The measured *P*-wave velocity reduces from 6 km/s for the most intact sample down to 4.2 km/s for pulverised samples at 5 MPa effective confining pressure. These values are in agreement with those measured by **?** on dynamically fractured samples of the same material, where *P*-wave velocity dropped down to 4 km/s, although measured without confining pressure. Lower velocities were observed in the pulverised samples and highest velocities in the least damaged samples. All velocities increase with effective pressure (Figure 4a). Pulverised samples are more sensitive to increasing pressure than fractured samples, as evidenced by the decreasing *P*-wave time-of-flight relative to the measurement at lowest effective pressure (Figure 4b).

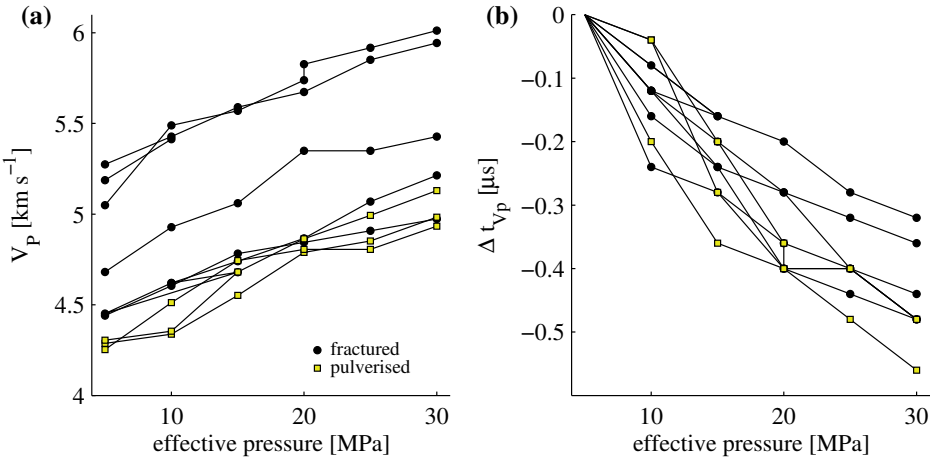

Figure 4: **(a)**: *P*-wave velocity (V_P) versus effective pressure for fractured (circles) and pulverised (open squares) samples. No distinction was made between single and successively loaded samples. **(b)**: Change in *P*-wave time-of-flight (Δt_{v_P}) relative to the measurement at lowest effective pressure for fractured and pulverised samples.

Sample #	$P_{eff\ [MPa]}$	Permeability [m^2]	
QM18	6.9	4.87E-17	>
QM18	12	3.49E-17	>
QM18	18.7	2.76E-18	>
QM18	22.6	2.51E-18	>
QM18	27.05	1.79E-18	>
QM18	32.12	8.90E-19	>
QM18	27.7	1.04E-18	<
QM18	22.9	1.24E-18	<
QM18	17.28	2.23E-18	<
QM18	12.75	8.56E-18	<
QM18	8	4.73E-18	<
QM12	6.2	9.26E-18	>
QM12	11.8	4.32E-18	>
QM12	17.2	1.89E-18	>
QM12	21.9	1.02E-18	>
QM12	27	5.80E-19	>
QM12	32.5	3.05E-19	>
QM12	27.1	3.01E-19	<
QM12	21.7	4.18E-19	<
QM12	16.95	4.67E-19	<
QM12	11.93	5.64E-19	<
QM12	7.2	9.32E-19	<
QM13	6.37	7.99E-19	>
QM13	12.85	4.32E-20	>
QM17	6.49	4.15E-14	>
QM17	12.36	2.54E-14	>
QM17	16.7	1.06E-14	>
QM17	21.73	5.45E-15	>
QM17	26.7	2.86E-15	>
QM17	31.85	3.20E-15	>
QM17	31.5	2.25E-15	<
QM17	26.9	1.92E-15	<
QM17	21.9	3.52E-15	<
QM17	17.06	2.82E-15	<
QM17	12.03	4.61E-15	<
QM17	7.2	5.52E-15	<
QM11	6.15	6.19E-15	>
QM11	11.92	3.39E-16	>
QM11	16.52	3.19E-16	>
QM11	21.5	6.40E-16	>
QM11	26.55	7.59E-16	>
GS03	5	8.73E-20	>
GS02	6.8	2.24E-15	>
GS02	7.8	1.54E-15	>
GS02	16.4	9.86E-16	>
GS02	23.1	2.40E-16	>
GS02	27.6	2.73E-16	>
GS02	33.3	1.52E-16	>
GS02	33.1	1.22E-16	<
GS02	26.4	1.34E-16	<
GS02	20.9	1.46E-16	<
GS02	12.6	1.62E-16	<
GS02	6.35	2.33E-16	<
QM16	6.63	2.63E-16	>
QM16	12.04	5.73E-17	>
QM16	16.9	2.12E-17	>
QM16	21.58	1.43E-17	>
QM16	26.55	8.33E-18	>
QM16	31.7	5.46E-18	>
QM16	26.89	7.63E-18	<
QM16	22.03	1.16E-17	<
QM16	16.8	2.69E-17	<
QM16	11.93	7.47E-17	<
QM16	7	3.58E-16	<
QM23	6.6	8.41E-15	>
QM23	11.62	9.28E-15	>
QM23	16.98	3.88E-14	>
QM23	16.98	2.77E-14	>
QM23	21.87	1.59E-14	>
QM23	26.7	1.11E-14	>
QM23	31.88	7.13E-15	>
QM23	27.01	1.72E-14	<
QM23	22.04	1.89E-14	<
QM23	17.72	2.18E-14	<
QM23	12.2	2.52E-14	<
QM23	7	2.96E-14	<
QM27	7.16	6.17E-14	>
QM27	16.44	6.16E-14	>
QM27	21.46	4.17E-14	>
QM27	26.63	2.89E-14	>
QM27	31.87	1.66E-14	>
QM27	27.42	1.28E-14	<
QM27	22.35	9.45E-15	<
QM27	17.18	7.79E-15	<
QM27	11.96	7.43E-15	<
QM27	6.85	8.15E-15	<
QM27	7.42	7.00E-15	>*
QM27	16.16	5.60E-15	>*
QM27	26.86	3.99E-15	>*
QM27	17.29	3.86E-15	<*
QM27	7.12	4.02E-15	<*
QM10	6.82	1.17E-15	>
QM10	12	1.39E-15	>
QM10	16.97	1.25E-15	>
QM10	22	1.58E-15	>
QM10	22	1.45E-14	>
QM10	27.11	1.66E-14	>
QM10	32.16	9.84E-15	>
QM10	27.22	1.30E-14	<
QM10	22.1	1.50E-14	<
QM10	17.01	1.23E-14	<
QM10	11.25	2.95E-15	<
QM10	7.15	5.24E-16	<

Table S1: Permeability at varying effective pressures measured during loading path (>) or unloading path (<). *: Second cycle of confining pressure loading.